

# A multi-coloured survey of NGC 253 with XMM-Newton: testing the methods used for creating luminosity functions from low-count data

R. Barnard<sup>1</sup>, L. Shaw Greening<sup>1</sup> and U. Kolb<sup>1</sup>

<sup>1</sup>*Department of Physics and Astronomy, The Open University, Walton Hall, Milton Keynes, MK7 6AA, UK*

## ABSTRACT

NGC 253 is a local, star-bursting spiral galaxy with strong X-ray emission from hot gas, as well as many point sources. We have conducted a spectral survey of the X-ray population of NGC 253 using a deep XMM-Newton observation. NGC 253 only accounts for  $\sim 20\%$  of the XMM-Newton EPIC field of view, allowing us to identify  $\sim 100$  X-ray sources that are unlikely to be associated with NGC 253. Hence we were able to make a direct estimate of contamination from e.g. foreground stars and background galaxies.

X-ray luminosity functions (XLFs) of galaxy populations are often used to characterise their properties. There are several methods for estimating the luminosities of X-ray sources with few photons. We have obtained spectral fits for the brightest 140 sources in the 2003 XMM-Newton observation of NGC 253, and compare the best fit luminosities of those 69 non-nuclear sources associated with NGC 253 with luminosities derived using other methods. We find the luminosities obtained from these various methods to vary systematically by a factor of up to three for the same data; this is largely due to differences in absorption. We therefore conclude that assuming Galactic absorption is probably unwise; rather, one should measure the absorption for the population.

A remarkable correlation has been reported between the XLFs of galaxies and their star formation rates. However, the XLFs used in that study were obtained using several different methods. If the sample galaxies were revisited and a single method were applied, then this correlation may become stronger still.

In addition, we find that standard estimations of the background contribution to the X-ray sources in the field are insufficient. We find that the background AGN may be systematically more luminous than previously expected. However, the excess in our measured AGN XLF with respect to the expected XLF may be due to an as yet unrecognised population associated with NGC 253.

**Key words:** X-rays: general – X-rays: binaries – Galaxies: individual: NGC 253

## 1 INTRODUCTION

The X-ray source populations of external galaxies have been well studied for the last  $\sim 20$  years (see e.g. Fabbiano 1989 2006; Read & Pietsch 2001; Kilgard et al. 2005, and references within). Historically, studies of the individual sources have been severely limited by low count rates and signal to noise. One approach is to analyse the colours of each source (see e.g. Lira et al. 2002; Prestwich et al. 2003). Alternatively, one may convert from intensity to flux using an assumed model, and then create an X-ray luminosity function (XLF) to characterise a galaxy or group of galaxies (e.g. Fabbiano 2006; Kilgard et al. 2005; Misanovic et al. 2006). This model may simply consist of a standard X-ray binary

emission model with Galactic line-of-sight absorption (see e.g. Zezas & Fabbiano 2002; Soria & Kong 2002); alternatively, the model may be obtained from fitting the whole X-ray population of a galaxy (e.g. Irwin et al. 2003), or splitting this population into several groups (e.g. Roberts et al. 2002). The X-ray point source population for an external galaxy is expected to be dominated by X-ray binaries, with a small fraction being supernova remnants.

Empirical relations exist that link the X-ray properties of a galaxy with their mass (Gilfanov 2004) and star formation rate (Grimm et al. 2003). However, observations of small or distant galaxies that account for a small portion of the field of view are dominated by X-ray sources that are unrelated to the target galaxy, such as foreground stars and

background galaxies. Hence, one must estimate the contribution of such sources to the galaxy's XLF before one can estimate its properties. Moretti et al. (2003) have performed one of the most comprehensive studies of the XLFs for the X-ray background to date. They analysed the data from a large number of deep and wide-field surveys with ROSAT, ASCA, XMM-Newton and Chandra. From these observations they constructed XLFs in a soft band (1–2 keV) and a hard band (2–10 keV), converting from intensity to flux via assumed emission models; these XLFs are normalised by area. Hence, one can estimate the contribution of such background sources to the XLF of a target galaxy by scaling these XLFs by the distance to, and the area covered by, the galaxy.

Using XMM-Newton, the most sensitive X-ray imaging telescope to date in the 0.3–10 keV band (Turner et al. 2001; Strüder et al. 2001), we can test the validity of these methods. We can do this by freely modelling individual X-ray sources in nearby galaxies, and comparing the resulting XLF with XLFs derived using the various methods described above. NGC 253 is ideal for this purpose, as NGC 253 is large ( $\sim 25' \times 7'$ ), but only fills  $\sim 20\%$  of the XMM-Newton field of view. Hence we may study the galaxy and the local background simultaneously.

NGC 253 is a star-bursting spiral galaxy in the Sculptor group that is almost edge on (inclination =  $78^\circ$ , Pence 1981). The distance to NGC 253 is uncertain, with measurements ranging from 2.58 Mpc (Puche et al. 1991) to 4 Mpc (Karachentsev et al. 2003). The X-ray population of NGC 253 is expected to be dominated by high mass X-ray binaries (HMXBs), because of the high star formation rate to mass ratio (see e.g. Grimm et al. 2003).

HMXBs are classified according to the donor star (see White et al. 1995, and references therein for a comprehensive review). Those with Be star donors have elliptical orbits with periods of hundreds of days, and only accrete near periastron, via the stellar wind (Bondi & Hoyle 1944); as a result, they are transient sources with luminosities generally  $\sim 10^{33}$ – $10^{36}$  erg s $^{-1}$ . In HMXBs containing supergiants (SG HMXBs), the donor star is either filling, or almost filling, its Roche lobe (see Kaper et al. 2004, for a review). The compact object in SG HMXBs is continuously accreting either via Bondi-Hoyle accretion or via an accretion disc; Bondi-Hoyle accretion yields luminosities in the range  $\sim 10^{33}$ – $10^{36}$  erg s $^{-1}$ , while disc accretion can power luminosities up to  $\sim 10^{38}$  erg s $^{-1}$ . Our survey is limited to bright X-ray sources, and hence we expect our sample to be dominated by disc-fed sources.

In this work we examine the 2003, June XMM-Newton observation of NGC 253. We first provide details of the observation and the data analysis in Sect. 2. We then present our results in Sect. 3. We first freely model the spectra of 140 bright X-ray sources, including 69 that we associate with NGC 253, and examine their group properties. We then compare the luminosities obtained from these spectral fits with luminosities obtained using several standard methods. Finally we compare the theoretical AGN XLF of Moretti et al. (2003) with the XLF derived from our freely fitted background sources. We discuss the implications of our findings in Sect. 4, particularly the implications for the empirical relation between the X-ray properties of a galaxy and its star formation rate, and the universal HMXB XLF proposed by

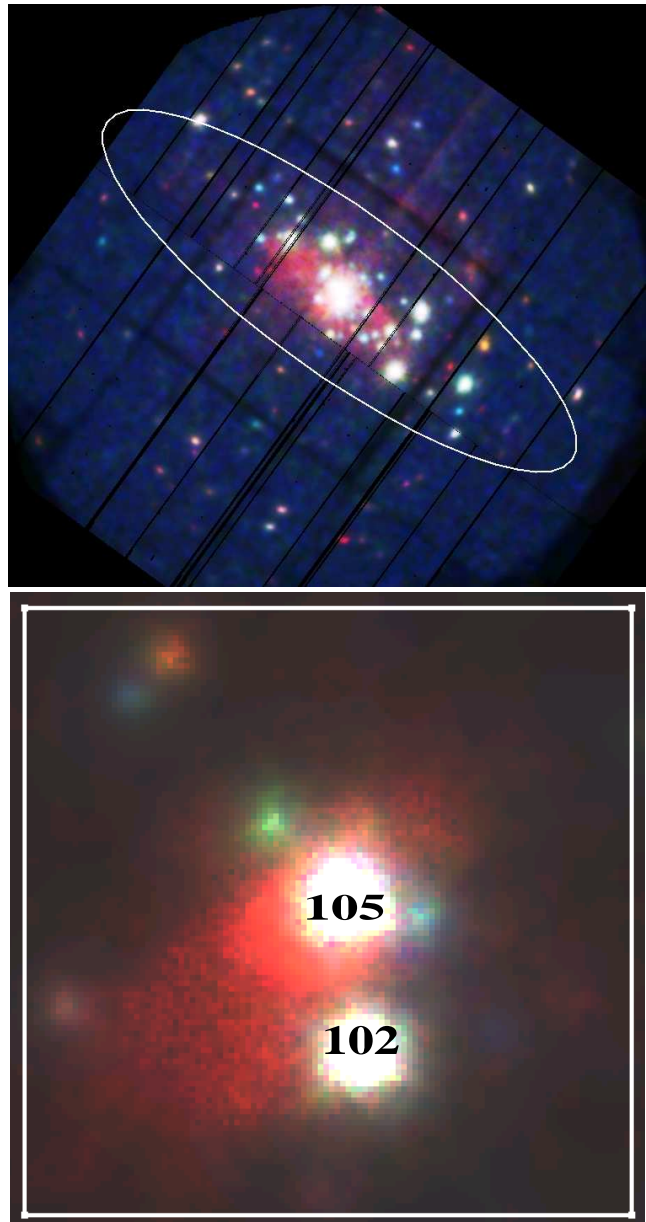


**Figure 1.** *Upper panel:* Three-colour, combined EPIC,  $\sim 30' \times 30'$  image from the 2003 XMM-Newton observation of NGC 253; the intensity scale is histogram equalised. North is up, East is left. The energy bands used were 0.3–2.0 keV (red), 2.0–4.0 keV (green) and 4.0–10.0 keV (blue). The white ellipse represents the V band D<sub>25</sub> contour of NGC 253. *Lower panel:* Linear-scaled image of the central  $2' \times 2'$  region; several point sources are visible, while the red smudge is the superwind reported by Pietsch et al. (2001). Source 105 is the nuclear region.

Grimm et al. (2003). Finally, we draw our conclusions in Sect. 5.

## 2 OBSERVATIONS AND DATA ANALYSIS

XMM-Newton observations are susceptible to periods of high background levels, caused by increased flux of solar particles. We screened the data from each of the EPIC cameras (MOS1, MOS2 and pn), to remove flaring intervals.

This process resulted in  $\sim 46$  ks of good time for the pn and  $\sim 69$  ks for the MOS cameras.

We combined the cleaned MOS and pn data, and ran the source detection algorithm provided with the XMM-Newton data analysis suite SAS version 7.0. We accepted sources with maximum likelihood detections  $>10$  (equivalent to  $4\sigma$ ). For every source, we obtained an extraction region with radius 12–40". In general, we used a radius of 20", except for sources with large PSFs due to high off-axis angle, where a 40" radius was used, or in very crowded regions, where a radius of 12–15" was used. The extraction radius for each source is provided in Table A1. The central region of NGC 253 is fairly crowded, and we ignored sources with another source  $<10''$  away. This resulted in the loss of only a few faint sources.

We also created a corresponding background region for every source. We required that the background be on the same CCD as the source for all three EPIC cameras, that there be no point sources in the background, and that its intensity per unit area be smaller than for the source region. The resulting background regions had areas 1–35 times greater than their corresponding source regions; for 75% of sources, the background area was more than three times larger than the source area.

We extracted pn and MOS source and background spectra in the 0.3–10 keV range, combining the MOS1 and MOS2 spectra if the source was present in both cameras. We obtained fits to all spectra with  $>50$  source counts in the pn and/or MOS spectra with XSPEC 11.3<sup>1</sup>. We used power law, blackbody and bremsstrahlung models; all models included line-of-sight absorption. We considered all fits with null hypothesis probability  $\geq 0.05$  as acceptable; this is the probability that the differences between the modelled and observed spectra are due to random fluctuations alone. If none of these spectral models provided a good fit, we considered a two-component model consisting of a power law and blackbody, as seen in Galactic X-ray binaries. We used the best fit model to obtain a 0.3–10 keV, unabsorbed flux for each source.

### 3 RESULTS

In Fig. 1 we present a three-colour, combined EPIC image ( $\sim 30' \times 30'$ ) from the 2003, June observation. The images were binned to  $2400 \times 2400$  pixels, then smoothed with the SAS task *asmooth*. The smoothed images were weighted by corresponding exposure maps. North is up, East is left. The white ellipse represents the V band  $D_{25}$  isophot for NGC 253. Both populations of X-ray sources, inside and outside the  $D_{25}$  isophot, clearly display a wide range of colours. We also show a linearly-scaled close-up of the central  $2' \times 2'$  region, showing several point sources in a region that looks like one unresolved source in the main image.

#### 3.1 Point source detection

Source detection revealed 185 point sources; they are designated S1–S185, and their locations are presented in Table A1

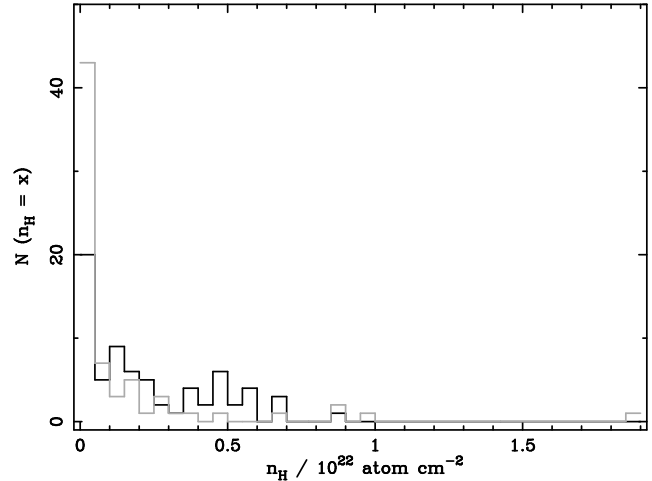


**Figure 2.** Histograms of best fit line-of-sight absorption,  $n_H$ , for the IS (black) and OS (grey) populations.

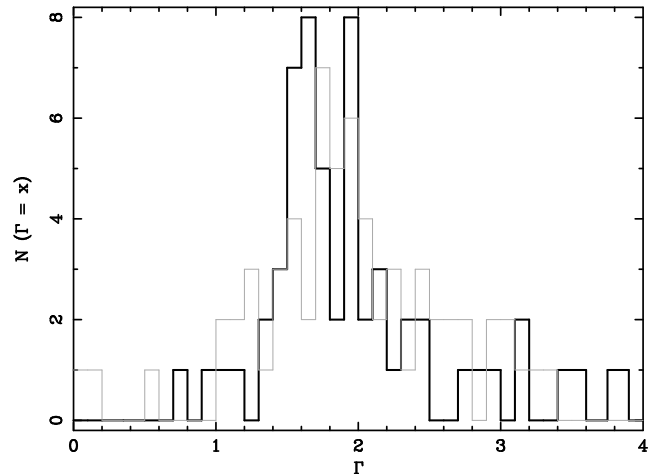


**Figure 3.** Histograms of best fit spectral index,  $\Gamma$ , for the IS (black) and OS (grey) populations.

in the Appendix. In this work we separate these sources into those inside and outside the  $D_{25}$  isophot of NGC 253, IS and OS respectively. We found 140 out of the 185 XMM-Newton sources in Chandra observations: 3 XMM-Newton detections contained multiple Chandra sources, but the other 137 are single point sources, as far as can be told by the current X-ray telescopes. Vogler & Pietsch (1999) identified S9, S65 and S163 as background QSOs via their optical counterparts; they also identified S100 as a foreground star. Vogler & Pietsch (1999) also labelled S102 as a possible black hole X-ray binary, due to its high luminosity.

We found no associations between our X-ray sources and the identified globular clusters; however, we found two X-ray sources that were within  $1''$  of globular cluster candidates (Beasley & Sharples 2000). One of these was S65, leaving just S166 as a possible globular cluster X-ray source. These results suggest that the population outside the  $D_{25}$  region are almost entirely unrelated to NGC 253, making it a good probe of the local X-ray background. However, we note that Galleti et al. (2004) have announced 380 globular

<sup>1</sup> <http://heasarc.nasa.gov/xanadu/xspec/>

**Table 1.** Best fit parameters for power law models applied to the summed spectra of the IS and OS faint source populations. We first show the number of faint sources in the population. We then show the best fit absorption and photon index, the  $\chi^2/\text{dof}$  and corresponding good fit probability, and the flux equivalent to 1 count  $\text{s}^{-1}$  in the 0.03–10 keV band for an extraction region with  $15''$  radius in the pn and MOS. Numbers in parentheses indicate 90% uncertainties in the last digit

Model	$N_{\text{Fnt}}$	$n_{\text{H}} / 10^{20}$	$\Gamma$	$\chi^2/\text{dof}$	Flux (pn thin)	Flux (MOS med)
IS	7	1.3	0.4(3)	71/54 [0.06]	1.1(2)E+4	3.6(8)E+4
OS	36	1.3	1.23(13)	55/44[0.12]	4800(400)	1.9(2)E+4

cluster candidates in NGC 253, but have yet to publish the results of their follow-up observations.

### 3.2 Spectral analysis

We found 71 IS and 69 OS sources to be bright enough for spectral modelling. Lightcurves of each source were checked for variability; the spectral models are only valid if the source is stable. Variability of sources in NGC 253 will be discussed in a following paper (Barnard et al. in prep).

Our strategy for obtaining spectra was designed to ensure at least 5–10 source counts per channel, favouring a few 10-count channels over many channels with less source counts. Spectra with  $>500$  source counts were grouped to a minimum of 50 counts per bin; those with 200–499 were grouped to a minimum of 20 counts per bin; those with 50–199 counts where the source contributed  $\geq 50\%$  of the total counts were binned to a minimum of 10 counts per bin; finally, sources with 50–199 counts where the source contribution  $< 50\%$  were grouped to a minimum of 20 counts per bin. We also note that the source + background spectrum always had at least 10 counts per channel by design, and that our large background regions ensured a good determination of the background spectrum. As a result, even sources with only 51 source counts could discriminate between models in some cases.

#### 3.2.1 Spectral properties of the bright X-ray sources

Here we compare the spectral properties of those sources bright enough for modelling. Details of each fit are presented in Table A2. We first looked at the range in line-of-sight absorption exhibited by these sources, then looked at the best fit photon index for a power law model, even for sources where a power law does not give the best fit. For this comparison we ignored S105 (the nuclear region) and S163 (an AGN) from the IS population, and S100 (a foreground star) from the OS population.

Figure 2 shows histograms of the line-of-sight absorption,  $n_{\text{H}}$ , for the IS (thick black) and OS (thin grey) populations, with a resolution of  $0.05 \times 10^{22}$  H atom  $\text{cm}^{-2}$ . We see that  $\sim 70\%$  of the IS population have absorptions  $> 5 \times 10^{20}$  H atom  $\text{cm}^{-2}$ , i.e.  $> 4$  times Galactic line-of-sight absorption ( $\sim 1.3 \times 10^{20}$  H atom  $\text{cm}^{-2}$ , Stark et al. 1992); indeed, 16 of the sources ( $\sim 25\%$ ) exhibit absorption  $> 40$  times Galactic absorption. This variation is perhaps unsurprising in a spiral galaxy that is almost edge on, particularly when one expects the X-ray sources in NGC 253 to be HMXBs, and therefore linked to regions of high star formation rate. Meanwhile, the

majority of the spectrally fitted OS sample, thought mostly to be background galaxies, have low absorptions. This is likely to be a selection effect, caused by choosing only the brightest (i.e. nearest, or least absorbed) galaxies.

Figure 3 shows the distribution in photon index,  $\Gamma$ , for the best fit power law models to the IS and OS populations. Again, the IS histogram is represented by a thick black line and the OS histogram by a thin grey line. Around 10% of sources exhibited thermal spectra, and yielded  $\Gamma > 4$ ; such sources were excluded from Fig. 3. While many published XLFs assume a single value of  $\Gamma$ , a broad range is observed in both the IS and OS populations.

#### 3.2.2 Modelling the faint sources

We classify those sources that are not bright enough for spectral modelling as faint sources. We separately summed the spectra of the 7 faint IS and 36 faint OS sources, and modelled each of the summed spectra with a best fit power law. Table 1 summarises these models. For each model, we give the best fit absorption and photon index, as well as the conversion from intensity to flux for each instrument in the 0.3–10 keV band. This conversion factor is defined as the unabsorbed flux equivalent to 1 count  $\text{s}^{-1}$  for an on-axis source with an extraction radius of  $15''$ . We initially used the HEASARC WebPIMMS software<sup>2</sup> to calculate the conversion factors for each model. However, we realised that WebPIMMS does not account for the variation in calibration throughout the lifetime of XMM-Newton. Hence, we obtained the conversion factors for the observation discussed here using an on-axis,  $15''$  source. We note that  $\Gamma = 0.4 \pm 0.3$  for the best fit IS power law model. This is consistent with the 0.3–10 keV spectra of faint NS+Be HMXBs accreting via Bondi-Hoyle accretion (where  $\Gamma \sim 0\text{--}1.5$ , White et al. 1995).

### 3.3 Luminosities of NGC 253 X-ray sources from different methods

#### 3.3.1 Defining the methods

For the 69 IS sources discussed in Sect. 3.2.1, we obtained fluxes from the source intensities using some of the methods employed in the literature when creating the XLFs of external galaxies.

For Method I, we assumed a standard emission model and Galactic line-of-sight absorption. We tried a 5 keV

<sup>2</sup> <http://heasarc.gsfc.nasa.gov/Tools/w3pimms.html>

**Table 2.** Best fit absorbed power law models used to obtain the conversion factors for Methods I–III; the conversion factor is the 0.3–10 keV unabsorbed flux equivalent to a 0.3–10 keV pn intensity of 1 count s<sup>−1</sup> from an on-axis source region with 15'' radius. For each model we give  $n_{\text{H}}$ ,  $\Gamma$ ,  $\chi^2/\text{dof}$  and conversion factor (0.3–10 keV unabsorbed flux in 10<sup>−15</sup> erg cm<sup>−2</sup> s<sup>−1</sup> equivalent to 1 count s<sup>−1</sup> in the pn from an on-axis source with 15'' radius).

	Model	$n_{\text{H}} / 10^{20} \text{ atom cm}^{-2}$	$\Gamma$	$\chi^2/\text{dof}$	Conversion Factor
	Model I: Standard model	1.3	1.7	9909/779	4006
	Model II: Best fit to all non-nuclear NGC 253 sources	34	2.49	1339/777	8252
	Model III: <3000 counts	19	2.40	665/495	5365
	Model III: >3000 counts	50	2.65	1795/1959	11693

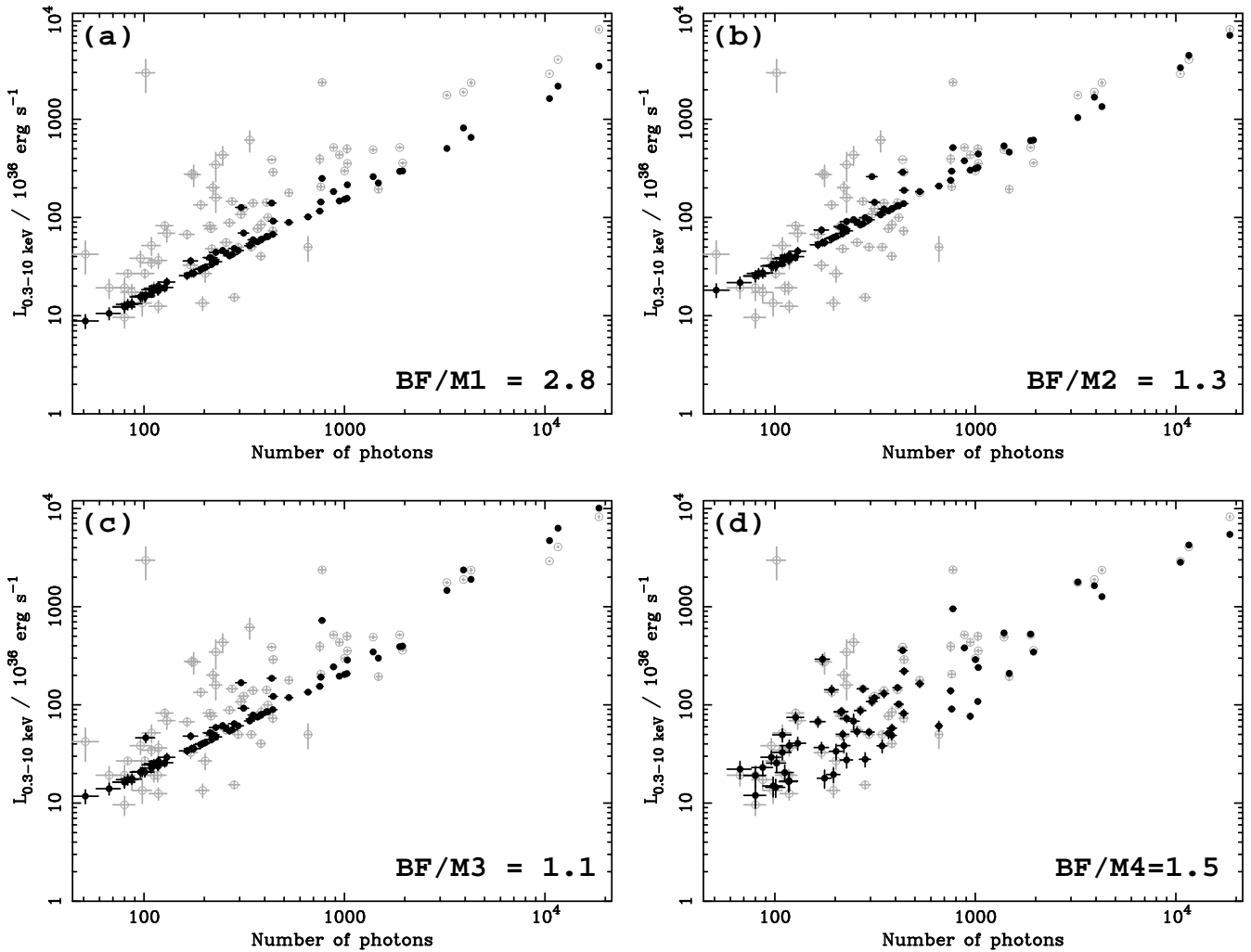


**Figure 4.** Comparison of luminosities obtained from best fits to 69 IS sources with luminosities obtained using Methods I–IV (panels a–d respectively) as a function of the number of pn source photons accumulated from the source. A distance of 4 Mpc is assumed. The best fit luminosities are grey, hollow circles, while luminosities derived using each method are dark, solid circles. For each model we give the ratio BF/M $x$ , where  $x$  is 1–4. This is the ratio of the summed 0.3–10 keV luminosity from the individual best fits to the summed 0.3–10 keV luminosity using Method I–IV.

bremsstrahlung model (see e.g. Zezas & Fabbiano 2002) as well as a power law with  $\Gamma = 1.7$  (see e.g. Soria & Kong 2002); we found the conversion factors for these models to agree within 3% for the pn and 5% for the MOS. We chose the power law model. For Method II, we combined the source regions for all of the sources, and obtained a com-

posite source spectrum; similarly, a composite background spectrum was obtained by adding all the background regions. The background-subtracted spectrum was then modelled by an absorbed power law, giving the conversion factor; this method is similar to that used by e.g. Irwin et al. (2003). Method III involved splitting the NGC 253 popu-

lation into sources with >3000 net counts and those with <3000 net counts. We then found the conversion factor for each group. This method is similar to that employed by e.g. Roberts et al. (2002). Finally, we modelled each source with constrained power law emission with  $\Gamma = 1.7$ , but with the absorption free to vary; the motivation was to investigate the importance of the emission spectrum in deriving the source luminosity. We call this Method IV. Luminosities were calculated assuming a distance of 4 Mpc, as favoured by Grimm et al. (2003).

### 3.3.2 Applying the conversion factors

In Table 2, we list the spectral models and conversion factors used for Methods I–III. For each model, we give  $n_H$ ,  $\Gamma$ , and  $\chi^2/\text{dof}$ , as well as the conversion factor. This conversion from source intensity to flux assumes an on-axis source with a  $15''$  radius; however, our source regions varied in radius from  $12''$ – $40''$ , and had off-axis angles of  $\sim 0$ – $14'$ . Hence, it was necessary to correct the source intensities for vignetting, and differences in encircled energy fraction (EEF). The background-subtracted source intensities obtained from XSPEC are already vignetting corrected, and only EEF correction was necessary. We calculated the EEF for every source as a function of radius and off-axis angle, weighted by energy over the 0.3–10 keV band. If  $I(R, \Theta)$  and  $E(R, \Theta)$  are respectively the intensity and EEF for a source region of radius  $R$  and off-axis angle  $\Theta$ , then

$$\frac{I(R, \Theta)}{E(R, \Theta)} = \frac{I(15, 0)}{E(15, 0)}, \quad (1)$$

hence

$$I(15, 0) = I(R, \Theta) \times \frac{E(15, 0)}{E(R, \Theta)}. \quad (2)$$

This work ensures that the same corrections for EEF and vignetting were applied for Methods I–IV as for the best fit spectra. We present the EEF for each source in Table A1.  $E(15, 0)$  was found to be 0.71 for the pn, 0.68 for MOS1 and 0.69 for MOS2.

### 3.3.3 Comparing the methods

In Fig. 4 we compare the best fit luminosities with luminosities derived from Methods I–IV as a function of pn source counts in panels (a)–(d) respectively. The best fit luminosities are shown as grey, open circles, while the luminosities derived from Methods I–IV are solid circles. For Methods I and II, the luminosities are expected to have a linear relation to the number of source counts, and the scatter is due to differences in encircled energy and vignetting corrections.

We also show the ratio of total best fit to modelled luminosity for each method (BF/M $x$ , where  $x$  is the method number from 1 to 4). The total luminosity from the best fit spectra is 2.8 times higher than the Model I luminosity for the same sources, 30% higher than for Model II, and 10% higher than for Model III. It is unsurprising that Model III is most successful at reproducing the freely fit luminosity, as we grouped the sources into two intensity groups and obtained two very different conversion factors. Hence the relationship between intensity and luminosity is clearly non-linear.

We note with interest that Model I, with a best fit

$\chi^2/\text{dof} \sim 13$ , is furthest from agreement with individual fits. Meanwhile, the best fit for the Model III sources with >3000 counts yields  $\chi^2/\text{dof} \sim 0.92$ , and BF/M3 for just those sources is just 1.03. These results show that reliable luminosities can only be obtained from models that reflect the data.

For low luminosity sources, the Method IV and best fit luminosities agree fairly well. This is to be expected, as many low-luminosity disc-accreting XBs exhibit spectra that are well characterised by  $\Gamma=1.7$ . However, at higher luminosities, Method IV tends to underestimate the luminosity. Again, this is expected, as higher luminosity XBs exhibit systematically softer spectra than low luminosity XBs; hence  $\Gamma=1.7$  is generally no longer a good fit. As a result, Method III and even Method II give a better estimate of the integrated luminosity of NGC 253.

## 3.4 Luminosity functions of the NGC 253 and background populations

While we associate the IS population with NGC 253, the OS population represents the background AGN. Before comparing the XLFs of the IS and OS populations, we normalised them by area. Assuming a circular field of view with  $15'$  radius, NGC 253 and the background region cover 137 and 570 square arcminutes respectively. We present the best-fit XLFs of the IS and OS populations in Fig. 5; the 0.3–10 keV luminosity is plotted on the x-axis, and the number of sources per square degree with higher fluxes given on the y-axis. The black lines represent the IS XLF, while the grey lines represent the OS XLF. These luminosities are calculated assuming a distance of 4 Mpc. It is clear that the IS population has considerably higher spatial density than the OS population. Figure 5 leads us to expect little contribution from the background above  $\sim 2 \times 10^{37} \text{ erg s}^{-1}$ .

We next compare the best fit IS XLF with those of Methods I–III in Fig. 6. Unsurprisingly, the XLFs of Methods II and III are flatter than the XLF of Method I, as the Method I luminosities are systematically lower than for Methods II and III. The universal XLF for HMXBs reported by Grimm et al. (2003) relied on published XLFs that were created using a variety of methods. Our results show that the systematic variations between methods is likely to have introduced extra uncertainties in their results; we discuss the implications of our results more fully in Sect. 4.2.

## 3.5 Assessing the AGN contribution

In Fig. 7 we compare the Moretti et al. (2003) XLFs with best fit OS XLFs in the 1–2 keV (soft) and 2–10 keV (hard) bands, including faint sources. For the faint sources, the OS model presented in Table 1 is used to convert from intensity to flux. We note that our OS sample is rather limited, and does not necessarily represent the AGN background as a whole. However, our best fit OS XLF suggests that AGNs contribute rather more to the high luminosity end of the hard XLF than predicted by Moretti et al. (2003); conversely, our background AGNs appear to contribute less to the soft XLF than predicted. We also note that the best fit OS XLFs are steeper than those calculated by Moretti et al. (2003). Our observed 2–10 keV XLF for luminosities greater

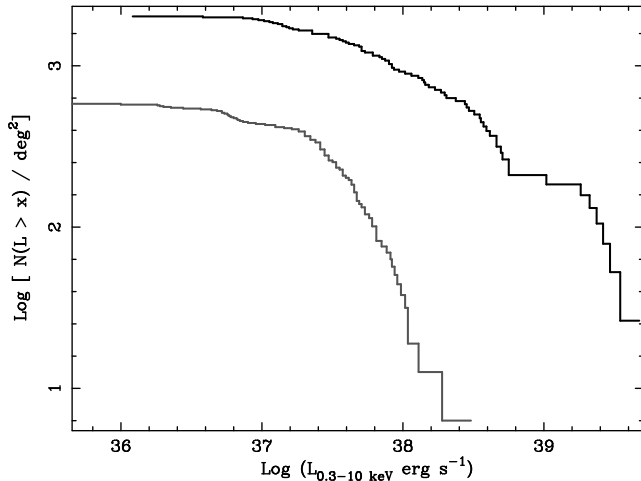


**Figure 5.** Best fit X-ray luminosity functions (XLFs) for the IS (black) and OS (grey) populations, assuming a distance of 4 Mpc. The nuclear source S105 and QSOs S163 and S26 are removed from the IS XLF. The foreground star S100 is removed from the OS XLF because it suffers 100% uncertainties. Kolmogorov-Smirnov (K-S) testing shows that the IS and OS populations have a probability of  $1.8 \times 10^{-7}$  for being drawn from the same population.

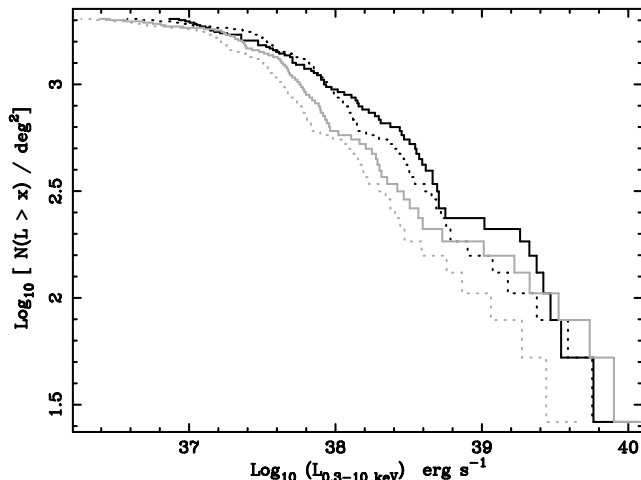


**Figure 6.** Comparison of best fit NGC 253 XLF (black, solid) with XLFs obtained using Method I (grey dotted), Method II (black, dotted) and Method III (grey, solid).

than  $\sim 10^{37} \text{ erg s}^{-1}$  suggests that the AGN are systematically more luminous than previously supposed; incompleteness prevents us from exploring the low luminosity end of the XLF. The observed excess could be due to an as yet unidentified population associated with NGC 253. However the lack of globular cluster associations to date makes this unlikely. Alternatively, the spectra of the AGN could simply be harder than assumed by Moretti et al. (2003), who assign an emission model to each source based on its intensity.

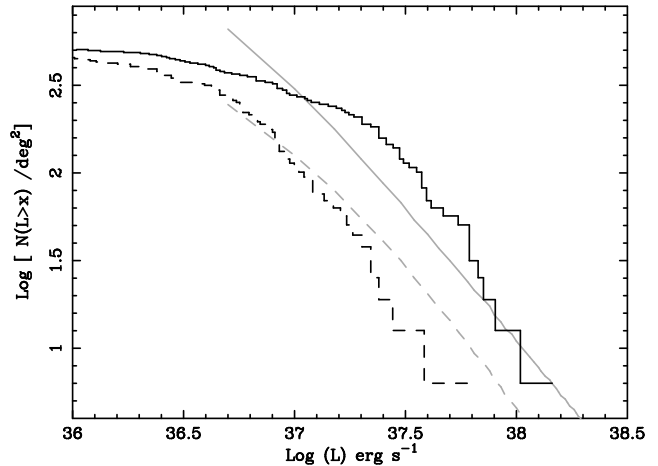


**Figure 7.** Comparison of the OS XLF (black) with the Moretti et al. (2003) XLFs (grey); 1–2 keV XLFs are represented by dotted lines, while the 2–10 keV LF is solid. The OS XLF includes sources that were too faint to fit individually, so the best fit power law to the summed faint source spectrum was used (see Table 1). The Moretti et al. (2003) XLFs were constructed from several surveys where fluxes were obtained by assuming a single spectral model for a given field. Our XLFs suggest that the true contribution of background AGN is higher in the 2–10 keV band, and somewhat lower in the 1–2 keV band, than is suggested by Moretti et al. (2003).

## 4 DISCUSSION

### 4.1 Comparing Methods I–IV

Absorption appears to be a major influence on the conversion factors for Models I–III; the modelled absorptions for Methods II and III are  $\sim 15$ –40 times higher than the Galactic line-of-sight absorption assumed for Method I. As a result, the luminosities obtained from Methods I–III vary by a factor of  $\sim 3$ . However, our results from Method IV show that absorption is not the only important influence in determining the source luminosity. We therefore conclude that one should not assume the absorption or emission spectra of extragalactic X-ray sources.

We expect many of the X-ray sources in NGC 253 to be disc-fed HMXBs. Galactic disc-fed LMXBs and HMXBs are known to exhibit softer spectra at higher luminosities, whether the accretor is a neutron star or black hole (see e.g. van der Klis 1994 1995; McClintock & Remillard 2003, and references within). Hence it is unsurprising that the relationship between counts and luminosity is non-linear. Subdivision of the X-ray population into intensity bands, and obtaining corresponding conversion factors (like Roberts et al., 2002), is therefore likely to be the best approach to fitting any low-photon-count data.

We note that Irwin et al. (2003) used an approach very similar to Method II for studying LMXBs in Chandra observations in nearby elliptical galaxies. They modelled the composite spectrum for each galaxy with an absorbed power law, but fixed the absorption in each case to Galactic values. They obtained good fits for each galaxy, with  $\Gamma$  ranging over  $\sim 1.4$ –1.9 between galaxies. These results suggest that using Galactic absorption and  $\Gamma = 1.7$  (i.e. Method I) is acceptable for LMXBs in elliptical galaxies. However, we would still recommend Method II (preferably Method III), in case

the X-ray population to be studied experiences absorption significantly higher than Galactic line-of-sight, or is systematically harder or softer than expected.

#### 4.2 Implications for the universal HMXB XLF

Grimm et al. (2003) used Chandra and ASCA surveys of nearby starburst galaxies, along with ASCA, MIR-KVANT/TTM and RXTE/ASM observations of HMXBs in our Galaxy and the Magellanic Clouds to obtain a correlation between the X-ray properties of HMXB populations and the star formation rate (SFR) of their host galaxies. They chose their sample of galaxies to have sufficiently high SFR to total mass ratios so that their X-ray populations would be dominated by HMXBs, with negligible LMXB contributions.

Grimm et al. (2003) used published Chandra XLFs, scaled to distances calculated from the radial velocities of Sandage & Tammann (1980), assuming the Hubble constant to be  $70 \text{ km s}^{-1} \text{ Mpc}^{-1}$ . They found the XLFs of these galaxies to be strikingly similar, when normalised by the SFR of the galaxy; estimates for the SFR were obtained from IR, UV,  $H_\alpha$  and radio observations.

Grimm et al. (2003) proposed a universal HMXB XLF, with the differential form

$$\frac{dN}{dL_{38}} = (3.3^{+1.1}_{-0.8}) \times \text{SFR} \times L_{38}^{-1.61 \pm 0.02}, \quad (3)$$

where  $L_{38}$  is the luminosity normalised to  $10^{38} \text{ erg s}^{-1}$ , and the SFR is measured in  $\text{M}_\odot \text{ yr}^{-1}$ . They also derived two empirical relations between the X-ray properties of their sample galaxies and the SFR. Firstly, they find that the number of sources with 2–10 keV luminosities  $> 2 \times 10^{38} \text{ erg s}^{-1}$  to be proportional to  $\text{SFR}^{1.06 \pm 0.07}$ . Secondly, they find a linear relation between the total HMXB X-ray flux of a galaxy and its SFR, for SFRs  $\gtrsim 4 \text{ M}_\odot \text{ yr}^{-1}$ ; at lower SFRs, they find the total luminosity to be proportional to  $\text{SFR}^{1.7}$ .

Grimm et al. (2003) included NGC 253 in a secondary sample of galaxies used to test their XLF-SFR relation. They obtained the integrated 2–10 keV luminosity of  $5 \times 10^{39} \text{ erg s}^{-1}$  from an RXTE observation, using the best fit to the integrated spectrum (a power law with  $\Gamma = 2.7$ ), and assuming a distance of 4 Mpc. The SFR estimates from the multi-wavelength observations varied from  $1.5 \text{ M}_\odot \text{ yr}^{-1}$  ( $H_\alpha$ ) to  $6.5\text{--}9.5 \text{ M}_\odot \text{ yr}^{-1}$  (FIR); Grimm et al. (2003) adopted a SFR of  $4 \text{ M}_\odot \text{ yr}^{-1}$ . Using their values, NGC 253 is considerably less luminous than predicted by their relations.

However, the XLFs used by Grimm et al. (2003) were created using several methods. Some were obtained assuming a standard emission model and Galactic absorption (e.g. Zezas & Fabbiano 2002; Soria & Kong 2002), while Kaaret (2001) used a single emission model derived from source colours. Eracleous et al. (2002) assumed Galactic absorption for their XLFs, but derived spectra of each source from their colour and intensity, while Lira et al. (2002) derived the absorption and emission characteristics of their sources from the source colours. Smith & Wilson (2001) derived their XLF from the best fit spectral models to the brightest X-ray sources, while Roberts et al. (2002) grouped their sources by intensity and derived conversion factors for each group.

Grimm et al. (2003) have shown a striking correlation

between the star formation rates and XLFs of different galaxies, although there is significant scatter in the correlation. However, our results have shown that one can obtain very different luminosities from the same data when using different methods. Hence the differences in the XLFs presented by Grimm et al. (2003) may be due to the different methods used in obtaining each XLF. If one were to revisit the galaxies surveyed by Grimm et al. (2003) and obtain the XLFs using only a single method (preferably Method III), then the correlation between XLF and star formation rate may be strengthened.

## 5 CONCLUSIONS

Grimm et al. (2003) report a universal HMXB XLF derived from published XLFs of several nearby galaxies. They also derive relations between the star formation rate and (i) the total luminosity of the point X-ray sources in the galaxies and (ii) the number of X-ray sources in a galaxy with 2–10 keV luminosity  $> 2 \times 10^{38} \text{ erg s}^{-1}$ . However, the published XLFs were produced using a number of methods, in most cases assuming Galactic line-of-sight absorption.

We have tested several of these models using a deep XMM-Newton observation of the nearby galaxy NGC 253, included in a secondary sample of Grimm et al. (2003). We obtained freely modelled luminosities for the 140 brightest sources in the field and also obtained the conversion factors from intensity to flux for some of these different models. We found them to vary by a factor of  $\sim 3$ . We found the biggest influence on the conversion factor to be the absorption, which varied by a factor of  $\sim 50$  between methods. Since the universal XLF and relations between SFR and X-ray properties were obtained using a mixture of methods, we suggest that reanalysing the sample with a single approach could yield even more striking relations.

It is possible that NGC 253 may represent a “worst case” for absorption effects, as it is almost edge on and has a high star formation rate. However we note that our early (unpublished) studies of XMM-Newton observations of NGC 300 show similar disparity between Method I and best fit luminosities; NGC 300 is almost face on and has a much lower star formation rate. Hence, our concerns about assuming Galactic absorption and standard emission models may apply to all galaxies to some extent.

Furthermore, we find that the background XLFs obtained by Hasinger et al. (2001) and Moretti et al. (2003) should be treated with caution and may be misleading. The true background XLF appears to contribute more to the high-flux sources, and correspondingly less to the lower fluxes. I.e., the high flux gradient is steeper, while the low flux gradient is flatter. Hence, the background XLFs also need to be re-calibrated using best fit models rather than assumed models.

It is not yet possible to combine the superlative spatial resolution of Chandra with the sensitivity of XMM, hence recalibrating the XLF-SFR relation, and the XLF for background AGN, will be difficult. However, we find that using an intensity to flux conversion that is derived from the best fit model to summed X-ray sources is more successful than just assuming a standard model. The more luminous X-ray sources are systematically softer than the fainter ones, hence



it makes sense to group X-ray sources by intensity, and apply the best fit to the summed spectrum of each group when converting from intensity to flux.

## ACKNOWLEDGMENTS

We gratefully thank the anonymous referee for their constructive comments. Astronomy research at the Open University is funded by a STFC rolling grant.

## REFERENCES

- Beasley, M. A. & Sharples, R. M. 2000, *MNRAS*, 311, 673  
 Bondi, H. & Hoyle, F. 1944, *MNRAS*, 104, 273  
 Eracleous, M., Shields, J. C., Chartas, G., & Moran, E. C. 2002, *ApJ*, 565, 108  
 Fabbiano, G. 1989, *ARA&A*, 27, 87  
 —. 2006, *ARA&A*, 44, 323  
 Galletti, S., Cacciari, C., Federici, L., et al. 2004, *Memorie della Societa Astronomica Italiana*, 75, 146  
 Gilfanov, M. 2004, *MNRAS*, 349, 146  
 Grimm, H.-J., Gilfanov, M., & Sunyaev, R. 2003, *MNRAS*, 339, 793  
 Hasinger, G., Altieri, B., Arnaud, M., et al. 2001, *A&A*, 365, L45  
 Irwin, J. A., Athey, A. E., & Bregman, J. N. 2003, *ApJ*, 587, 356  
 Kaaret, P. 2001, *ApJ*, 560, 715  
 Kaper, L., van der Meer, A., & Tijani, A. H. 2004, in *Revista Mexicana de Astronomia y Astrofisica Conference Series*, Vol. 21, *Revista Mexicana de Astronomia y Astrofisica Conference Series*, ed. C. Allen & C. Scarfe, 128–131  
 Karachentsev, I. D., Grebel, E. K., Sharina, M. E., et al. 2003, *A&A*, 404, 93  
 Kilgard, R. E., Cowan, J. J., Garcia, M. R., et al. 2005, *ApJS*, 159, 214  
 Lira, P., Ward, M., Zezas, A., Alonso-Herrero, A., & Ueno, S. 2002, *MNRAS*, 330, 259  
 McClintock, J. E. & Remillard, R. A. 2003, *Compact Stellar X-ray Sources* (Cambridge University Press), in press, astro-ph/0306213  
 Misanovic, Z., Pietsch, W., Haberl, F., et al. 2006, *A&A*, 448, 1247  
 Moretti, A., Campana, S., Lazzati, D., & Tagliaferri, G. 2003, *ApJ*, 588, 696  
 Pence, W. D. 1981, *ApJ*, 247, 473  
 Prestwich, A. H., Irwin, J. A., Kilgard, R. E., et al. 2003, *ApJ*, 595, 719  
 Puche, D., Carignan, C., & van Gorkom, J. H. 1991, *AJ*, 101, 456  
 Read, A. M. & Pietsch, W. 2001, *A&A*, 373, 473  
 Roberts, T. P., Warwick, R. S., Ward, M. J., & Murray, S. S. 2002, *MNRAS*, 337, 677  
 Sandage, A. & Tammann, G. A. 1980, *A revised Shapley-Ames Catalog of bright galaxies* (Washington: Carnegie Institution, 1980, Preliminary version)  
 Smith, D. A. & Wilson, A. S. 2001, *ApJ*, 557, 180  
 Soria, R. & Kong, A. K. H. 2002, *ApJL*, 572, L33

- Stark, A. A., Gammie, C. F., Wilson, R. W., et al. 1992, *ApJs*, 79, 77  
 Strüder, L., Briel, U., Dennerl, K., et al. 2001, *A&A*, 365, L18  
 Turner, M. J. L., Abbey, A., Arnaud, M., et al. 2001, *A&A*, 365, L27  
 van der Klis, M. 1994, *ApJs*, 92, 511  
 —. 1995, *X-ray Binaries* (Cambridge University Press), 256–307  
 Vogler, A. & Pietsch, W. 1999, *A&A*, 342, 101  
 White, N. E., Nagase, F., & Parmar, A. N. 1995, *X-ray Binaries* (Cambridge University Press)  
 Zezas, A. & Fabbiano, G. 2002, *ApJ*, 577, 726

## APPENDIX A: SOURCE DATA

In this section, we present positional information and spectral fits in Tables A1 and A2 for the 185 sources. Table A1 provides the right ascension and declination of each source in 2000 coordinates; these coordinate are not astrometrically corrected, but were taken directly from the source detection routine. We next indicate whether the source is in the D<sub>25</sub> isophot of NGC 253, the source extraction radius, background to source area ratio and the encircled energy fraction. Table A2 provides spectral information for each source. We give the best fit emission model for sources with >50 source counts in either their pn or MOS spectrum: power law (PO), blackbody (BB) or bremsstrahlung (BR); if the source is too faint for individual fitting, we show the faint source model applies (OS or IS, see Table 1). If an emission model was fitted, then we give the line-of-sight absorption,  $n_{\text{H}}^{22}$ , normalised to an equivalent density of  $10^{22}$  H atom cm<sup>-2</sup>; if the  $n_{\text{H}}$  falls below the Galactic absorption measured by Stark et al. (1992),  $0.013 \times 10^{22}$ , then the absorption is fixed at this value, indicated by 'f'. The best fit parameter is next, either  $\Gamma$  for power law models or kT (in keV) for blackbody or bremsstrahlung models. The best fit  $\chi^2/\text{dof}$  is shown next, with the good fit probability given in square brackets; we only accept models where the good fit probability >0.05. Finally, we give the best fit luminosity and the luminosity assuming a standard model. Some models have the minimum number of counts per bin quoted in parentheses, e.g. PO(30). This indicates that the spectrum had non-standard grouping. Such grouping was done if the standard grouping for a spectrum resulted in a data point that was unusually high or low as an artefact of grouping; grouping the spectrum to e.g. a minimum of 30 counts per bin rather than 50 counts per bin removes the artefact, showing that this outlier is not intrinsic to the source.

This paper has been typeset from a  $\text{\TeX}$ /  $\text{\LaTeX}$  file prepared by the author.

**Table A1.** Positions of X-ray sources in the XMM-Newton observations of NGC 253, along with some observed properties. Column 4 indicates whether the source is within the D<sub>25</sub> region of NGC 253. In Columns 5 and 6, we present the source extraction radius and background to source area ratio respectively. The encircled energy fraction is given for each source region in Column 7..

Source	$\alpha$	$\delta$	In D <sub>25</sub> ?	R <sub>s</sub>	A <sub>b</sub> / A <sub>s</sub>	EEF
1	0 46 27.12	−25 21 21.6	n	20	5.55	0.72
2	0 46 27.74	−25 19 26.76	n	20	5.55	0.75
3	0 46 36.22	−25 17 10.32	n	20	5.55	0.75
4	0 46 36.24	−25 20 23.64	n	20	5.55	0.75
5	0 46 38.83	−25 12 28.44	n	20	0	0.00
6	0 46 43.56	−25 19 35.04	n	20	5.55	0.75
7	0 46 44.64	−25 22 35.76	n	20	4.33	0.76
8	0 46 46.39	−25 25 53.4	n	20	12.17	0.75
9	0 46 47.4	−25 21 50.4	n	20	4.33	0.76
10	0 46 48.5	−25 11 47.4	n	20	10.18	0.76
11	0 46 49.01	−25 12 29.16	n	20	10.18	0.76
12	0 46 51.17	−25 27 30.24	n	20	10.18	0.75
13	0 46 55.99	−25 9 42.48	n	20	10.18	0.00
14	0 46 56.47	−25 20 34.8	y	20	5.02	0.77
15	0 46 56.54	−25 12 51.12	n	20	10.18	0.76
16	0 46 56.64	−25 28 39.36	n	20	10.18	0.75
17	0 46 56.86	−25 19 1.56	n	20	5.02	0.77
18	0 46 57.1	−25 30 26.28	n	20	5.02	0.75
19	0 46 57.43	−25 17 43.8	n	20	2.03	0.77
20	0 46 59.42	−25 28 46.2	n	20	10.18	0.75
21	0 46 59.57	−25 22 54.12	y	20	12.17	0.76
22	0 47 0.72	−25 18 33.84	n	20	5.02	0.77
23	0 47 0.96	−25 11 16.44	n	20	10.18	0.70
24	0 47 1.32	−25 23 25.44	y	20	12.17	0.76
25	0 47 1.99	−25 29 29.04	n	20	10.18	0.75
26	0 47 2.16	−25 24 24.84	y	20	12.17	0.76
27	0 47 3.53	−25 28 51.96	n	20	10.18	0.75
28	0 47 5.04	−25 29 36.24	n	20	10.18	0.75
29	0 47 5.38	−25 19 42.96	y	20	5.02	0.77
30	0 47 5.98	−25 22 27.12	y	20	5.02	0.77
31	0 47 6.62	−25 21 27.72	y	15	8.92	0.70
32	0 47 6.82	−25 9 11.16	n	20	5.02	0.76
33	0 47 6.98	−25 32 22.92	n	40	1.25	0.86
34	0 47 7.06	−25 15 48.24	n	20	2.36	0.77
35	0 47 8.14	−25 16 24.96	n	20	8.69	0.77
36	0 47 9.07	−25 17 39.12	y	20	2.64	0.77
37	0 47 9.1	−25 21 24.12	y	20	5.02	0.77
38	0 47 9.5	−25 14 4.56	n	20	12.53	0.77
39	0 47 10.22	−25 22 33.96	y	20	5.02	0.77
40	0 47 10.63	−25 16 31.08	n	20	8.69	0.78
41	0 47 11.09	−25 23 33	y	20	5.06	0.62
42	0 47 11.57	−25 10 41.16	n	20	5.02	0.77
43	0 47 11.98	−25 20 39.12	y	20	8.69	0.78
44	0 47 11.98	−25 17 43.44	y	20	1	0.77
45	0 47 14.14	−25 29 59.28	n	20	1.47	0.75
46	0 47 15.41	−25 12 0.36	n	20	4	0.77
47	0 47 15.74	−25 21 46.44	y	20	1	0.77
48	0 47 16.1	−25 23 38.76	y	20	5.06	0.77
49	0 47 16.9	−25 30 55.44	n	20	14.06	0.75
50	0 47 17.5	−25 18 10.43	y	10	24.5	0.58
51	0 47 17.52	−25 18 31.47	y	10	34.75	0.58
52	0 47 17.83	−25 25 26.76	n	20	5.06	0.77
53	0 47 18.26	−25 10 6.6	n	20	5.02	0.77
54	0 47 18.46	−25 19 14.88	y	20	4	0.78
55	0 47 18.78	−25 21 15.25	y	20	4	0.78
56	0 47 19.73	−25 6 45	n	20	6.68	0.76
57	0 47 20.14	−25 23 31.56	y	20	2.6	0.57
58	0 47 20.33	−25 13 18.48	n	20	3.52	0.78
59	0 47 20.45	−25 25 44.76	n	20	5.06	0.77
60	0 47 20.88	−25 17 48.48	y	20	8.69	0.78

Table A1. continued

Source	$\alpha$	$\delta$	In D <sub>25</sub> ?	R <sub>s</sub>	A <sub>b</sub> / A <sub>s</sub>	EEF
61	0 47 20.98	−25 10 1.2	n	20	2.48	0.77
62	0 47 22.15	−25 19 35.76	y	15	3.42	0.71
63	0 47 22.37	−25 12 1.44	n	20	2.48	0.78
64	0 47 22.56	−25 20 51.36	y	20	4	0.78
65	0 47 23.09	−25 10 55.2	n	20	4	0.77
66	0 47 23.26	−25 30 8.64	n	20	5.78	0.76
67	0 47 23.4	−25 19 5.88	y	15	3.42	0.64
68	0 47 23.76	−25 15 55.8	y	20	2.65	0.78
69	0 47 24.31	−25 14 50.64	y	20	2.65	0.78
70	0 47 24.96	−25 18 33.51	y	20	1.93	0.78
71	0 47 25.06	−25 19 47.28	y	20	1.93	0.54
72	0 47 25.08	−25 21 23.76	y	20	7.47	0.76
73	0 47 25.32	−25 16 43.68	y	20	3.15	0.78
74	0 47 25.42	−25 5 8.16	n	20	6.68	0.72
75	0 47 25.46	−25 28 48.72	n	20	5.78	0.76
76	0 47 25.94	−25 20 31.92	y	20	3.52	0.76
77	0 47 25.97	−25 8 16.8	n	20	6.68	0.75
78	0 47 26.06	−25 33 46.44	n	40	2.85	0.85
79	0 47 26.28	−25 15 56.16	y	20	4	0.78
80	0 47 26.4	−25 19 14.52	y	15	3.42	0.71
81	0 47 26.71	−25 7 38.28	n	20	6.68	0.76
82	0 47 27.43	−25 31 9.12	n	20	5.78	0.75
83	0 47 27.58	−25 12 20.88	n	20	2.48	0.78
84	0 47 27.77	−25 26 44.52	n	20	4	0.74
85	0 47 27.88	−25 18 17.05	y	20	2.1	0.66
86	0 47 28.22	−25 11 42	n	20	1.37	0.78
87	0 47 28.44	−25 9 24.48	n	20	2.11	0.77
88	0 47 28.56	−25 10 5.53	n	20	2.11	0.77
89	0 47 28.72	−25 19 23.52	y	15	2.08	0.71
90	0 47 28.82	−25 16 45.47	y	15	5.6	0.71
91	0 47 28.99	−25 28 10.2	n	20	5.78	0.76
92	0 47 29.76	−25 21 21.6	y	20	7.47	0.78
93	0 47 30.07	−25 17 1.32	y	15	5.6	0.71
94	0 47 30.24	−25 8 45.96	n	20	2.11	0.76
95	0 47 30.5	−25 11 29.4	n	20	1.55	0.56
96	0 47 30.74	−25 18 57.24	y	15	5.6	0.69
97	0 47 30.96	−25 18 27.36	y	15	5.6	0.71
98	0 47 31.25	−25 15 3.96	y	20	3.15	0.78
99	0 47 31.49	−25 10 1.2	n	20	2.2	0.76
100	0 47 32.4	−25 28 10.2	n	20	5.78	0.74
101	0 47 32.45	−25 31 14.88	n	20	5.78	0.75
102	0 47 32.98	−25 17 49.92	y	12	4.05	0.64
103	0 47 33	−25 18 45.72	y	15	5.6	0.71
104	0 47 33.31	−25 17 22.2	n	20	5.78	0.76
105	0 47 33.31	−25 30 19.44	y	12	8.75	0.64
106	0 47 33.48	−25 9 9.72	n	20	2.11	0.77
107	0 47 33.57	−25 16 33.93	y	20	3.15	0.79
108	0 47 35.04	−25 19 13.44	y	20	3.15	0.74
109	0 47 35.11	−25 15 12.24	y	20	3.15	0.79
110	0 47 35.45	−25 9 35.28	n	20	2.11	0.77
111	0 47 35.71	−25 16 31.8	y	20	3.15	0.79
112	0 47 36.1	−25 23 58.2	n	20	6.89	0.78
113	0 47 37.01	−25 10 42.24	n	20	2.36	0.77
114	0 47 37.08	−25 20 3.48	y	20	8.85	0.78
115	0 47 38.18	−25 15 43.2	y	20	3.07	0.79
116	0 47 38.98	−25 15 2.16	y	20	3.07	0.79
117	0 47 39.43	−25 16 32.88	y	20	3.07	0.79
118	0 47 40.15	−25 25 32.88	n	20	5.7	0.77
119	0 47 40.32	−25 17 57.84	y	20	1.03	0.79
120	0 47 40.73	−25 14 11.4	y	20	5.97	0.67

**Table A1.** continued

Source	$\alpha$	$\delta$	In D <sub>25</sub> ?	R <sub>s</sub>	A <sub>b</sub> / A <sub>s</sub>	EEF
121	0 47 41.33	−25 16 4.44	y	20	3.07	0.79
122	0 47 41.95	−25 17 20.04	y	20	3.07	0.79
123	0 47 42.51	−25 14 58.97	y	15	10.61	0.37
124	0 47 42.94	−25 9 56.52	n	20	1.56	0.77
125	0 47 42.96	−25 13 22.08	y	20	5.97	0.74
126	0 47 43.01	−25 15 30.25	y	15	2.78	0.29
127	0 47 43.3	−25 6 46.44	n	20	9	0.77
128	0 47 44.42	−25 26 51	n	20	5.7	0.77
129	0 47 44.64	−25 20 45.6	n	20	8.85	0.78
130	0 47 44.86	−25 14 55.3	y	15	10.61	0.71
131	0 47 45.05	−25 16 45.12	y	20	3.07	0.78
132	0 47 45.1	−25 12 21.24	y	20	5.97	0.78
133	0 47 45.79	−25 22 31.8	n	20	9.55	0.78
134	0 47 46.66	−25 27 35.64	n	20	3.07	0.76
135	0 47 46.73	−25 7 35.73	n	20	9	0.77
136	0 47 46.86	−25 29 55.68	n	40	1.43	0.81
137	0 47 46.92	−25 8 13.92	n	20	9	0.77
138	0 47 47.21	−25 6 30.96	n	20	9	0.76
139	0 47 48.26	−25 15 3.96	y	20	5.97	0.76
140	0 47 48.34	−25 9 5.04	n	20	9	0.77
141	0 47 48.7	−25 12 50.4	y	20	5.97	0.78
142	0 47 48.86	−25 16 28.92	y	20	0	0.77
143	0 47 49.06	−25 18 10.08	y	20	8.85	0.78
144	0 47 49.27	−25 23 8.52	n	20	9.55	0.78
145	0 47 49.32	−25 13 35.76	y	20	5.97	0.78
146	0 47 50.11	−25 6 59.04	n	20	9	0.77
147	0 47 50.28	−25 8 41.64	n	20	9	0.77
148	0 47 51.31	−25 10 23.16	n	20	2.93	0.58
149	0 47 51.6	−25 24 16.2	n	20	4.73	0.77
150	0 47 52.06	−25 17 32.28	y	20	9.77	0.78
151	0 47 52.85	−25 7 33.96	n	20	9	0.76
152	0 47 53.5	−25 13 8.04	y	20	3.02	0.78
153	0 47 55.15	−25 31 1.92	n	20	5.7	0.75
154	0 47 55.35	−25 19 6.82	n	20	9.77	0.66
155	0 47 56.4	−25 16 18.84	y	20	9.77	0.78
156	0 47 57.1	−25 15 3.24	y	20	0	0.78
157	0 47 57.22	−25 15 46.41	y	20	9.77	0.54
158	0 47 58.01	−25 29 48.48	n	20	5.7	0.76
159	0 47 58.22	−25 12 16.92	n	20	4.73	0.77
160	0 47 58.25	−25 26 4.2	y	20	2.93	0.75
161	0 47 58.73	−25 9 19.44	n	20	10.99	0.76
162	0 47 58.92	−25 30 55.44	n	20	5.7	0.75
163	0 48 0.07	−25 9 53.64	y	20	10.99	0.77
164	0 48 1.01	−25 23 46.65	n	20	5.1	0.77
165	0 48 1.22	−25 24 26.31	n	20	5.1	0.72
166	0 48 1.27	−25 27 37.44	n	20	4.73	0.76
167	0 48 2.09	−25 15 6.84	y	20	1	0.73
168	0 48 2.38	−25 11 25.8	y	20	10.99	0.77
169	0 48 3.79	−25 12 12.96	y	20	10.99	0.77
170	0 48 5.76	−25 25 51.6	n	20	5.1	0.7
171	0 48 6.6	−25 12 45	y	20	10.99	0.77
172	0 48 7.82	−25 14 17.52	n	20	5.1	0.77
173	0 48 7.87	−25 25 7.32	y	20	7.59	0.77
174	0 48 8.28	−25 22 57.36	n	20	11.78	0.73
175	0 48 9.26	−25 29 42.36	n	20	9	0.69
176	0 48 9.46	−25 29 3.84	n	20	9	0.7
177	0 48 14.09	−25 19 8.92	n	20	2.56	0.77
178	0 48 14.52	−25 13 20.64	y	20	7.59	0.77
179	0 48 18.48	−25 13 15.96	n	20	7.59	0.77
180	0 48 18.84	−25 15 8.28	n	20	7.59	0.77

Table A1. continued

Source	$\alpha$	$\delta$	In D <sub>25</sub> ?	R <sub>s</sub>	A <sub>b</sub> / A <sub>s</sub>	EEF
181	0 48 18.98	−25 14 21.48	n	20	7.59	0.77
182	0 48 23.04	−25 19 12.36	n	20	11.1	0.77
183	0 48 24.53	−25 18 11.16	n	20	11.1	0.76
184	0 48 31.25	−25 23 51	n	20	11.78	0.76
185	0 48 33.36	−25 15 19.25	n	40	1.18	0.11

**Table A2.** Spectral properties for each source. For each source we show the net counts in the pn and MOS detectors. We show the best fit model, absorption, parameter (spectral index or temperature),  $\chi^2/\text{dof}$  and good fit probability, best fit luminosity and standard model (Method I) luminosity. Best fit models for bright sources can be a power law (PO), blackbody (BB), bremsstrahlung (BR), or a two component model consisting of a blackbody plus power law (2C). Faint sources are modelled using a best fit power law listed in Table 1. Numbers in parentheses represent uncertainties in the last digit at the 90% confidence level. The quality of the spectrum may be deduced from the number of degrees of freedom because the spectra are grouped to a minimum number of counts per bin (brighter sources have more degrees of freedom).

S	pn source counts	MOS source counts	Mod	$n_{\text{H}}^{22}$	Par	$\chi^2/\text{dof}$ [gf]	$L_{36}^{\text{BF}}$	$L_{36}^{\text{SM}}$
1	48	0	OS				11.6(13)	8.04
2	27	0	OS				6.3(7)	4.35
3	0	0	X					0
4	34	3	OS				7.8(8)	5.43
5	0	0	X					0
6	57	68	PO	0.09(9)	2.5(12)	2/8 [0.92]	27(12)	9.16
7	53	31	PO	0.4(4)	2.3(1.9)	0.5/3 [0.915]	46(30)	8.43
8	57	30	PO	f	1.9(13)	6/4 [0.18]	29(27)	9.11
9	709	596	PO	f	1.9(9)	18/23 [0.78]	240(33)	112.64
10	33	76	PO	f	1.3(5)	5/5 [0.46]	46(30)	5.23
11	41	60	PO	f	2.1(7)	0.5/3 [0.915]	50(25)	6.48
12	0	0	X					0
13	0	0	X					0
14	164	129	PO	0.13(11)	1.8(4)	38/43 [0.67]	67(19)	25.73
15	359	306	PO	0.10(5)	1.83(17)	39/37 [0.39]	150(30)	56.39
16	0	0	X					0
17	53	28	PO	f	0.2(1.4)	8/6 [0.27]	40(30)	8.3
18	96	0	PO	f	1.7(6)	12/15 [0.69]	61(35)	15.47
19	154	124	PO	0.24(13)	2.6(6)	46/38 [0.18]	51(15)	24.09
20	0	21	OS				5.9(6)	4.09
21	109	61	PO	f	1.0(3)	32/22 [0.07]	52(29)	17.13
22	36	33	OS				8.1(9)	5.62
23	49	52	PO	f	2.7(12)	3 / 4 [0.63]	19(13)	8.4
24	118	98	PO	f	1.6(3)	35/34 [0.44]	36(17)	18.54
25	5	0	OS				1.15(13)	0.8
26	67	58	PO	f	2.2(5)	5/10 [0.88]	19(12)	10.55
27	30	16	OS				6.9(8)	4.78
28	10	0	OS				2.3(3)	1.6
29	1034	930	PO	0.17(3)	2.9(2)	41/35 [0.24]	355(38)	161.92
30	102	79	BB	0.7(3)	0.08(2)	8/6 [0.25]	2976(2972)	15.94
31	96	112	PO	f	1.2(2)	29/28 [0.42]	38(19)	16.46
32	119	0	PO	0.3(2)	2.3(8)	8/10 [0.58]	52(19)	18.71
33	181	0	PO	f	1.8(4)	12/24 [0.98]	90(46)	25.36
34	118	65	PO	0.12(11)	2.5(11)	16/20 [0.73]	27(12)	18.33
35	326	184	PO	0.04(4)	2.3(4)	35/40 [0.70]	61(12)	50.58
36	51	42	PO	0.4(4)	0.10(6)	1/6 [0.99]	42(42)	7.91
37	3244	3464	PO	0.53(10)	0.71(10) 2.0(2)	117/117 [0.48]	1762(135)	504.88
38	524	323	PO	f	2.30(12)	35/27 [0.15]	84(15)	81.38
39	192	161	PO	0.13(13)	0.8(6)	50/50[0.49]	134(38)	29.93
40	28	14	OS				6.3(7)	4.34
41	434	489	PO	0.18(4)	1.66(16)	34/47 [0.92]	388(25)	84.01
42	130	0	PO	0.19(16)	2.2(6)	13/10 [0.20]	42(15)	20.3
43	34	38	IS				14(3)	5.26
44	221	174	BB	0.5(2)	0.12(3)	45/40 [0.26]	202(83)	34.52
45	0	7	OS				1.89(19)	1.39
46	184	24	PO	0.08(8)	1.8(5)	34/31 [0.34]	44(13)	28.58
47	267	199	PO	0.07(7)	1.5(3)	33/45 [0.90]	88(21)	41.62
48	26	22	IS				11(2)	4.05
49	50	0	PO	f	0.13(5)	4/4 [0.44]	12(10)	8
50	3924	4144	PO	0.38(8)	2.10(8)	158/133 [0.07]	1890(150)	816.53
51	882	814	PO	0.43(6)	2.48(17)	30/28 [0.36]	516(65)	183.53
52	65	54	PO	0.5(4)	2.7(12)	8/12 [0.75]	27(12)	10.17
53	154	177	PO	0.30(18)	1.4(4)	38/37 [0.45]	83(25)	24
54	1001	1002	PO	0.12(3)	1.51(8)	46/42 [0.32]	297(34)	154.34
55	0	0	X					0
56	171	167	BB	f	0.193(16)	49/58	25(8)	26.93
57	31	91	PO	0.6(5)	2.8(10)	0.4/6 [0.999]	56(21)	6.55

Table A2. continued

S	pn source counts	MOS source counts	Mod	$n_{\text{H}}^{22}$	Par	$\chi^2/\text{dof}$ [gf]	$L_{36}^{\text{BF}}$	$L_{36}^{\text{SM}}$
58	235	71	BB	f	0.20(2)	40/28 [0.07]	19(6)	36.3
59	145	81	PO	0.04(4)	2.8(8)	33/29 [0.26]	27(10)	22.69
60	216	256	PO	0.23(13)	1.6(3)	45/36 [0.14]	77(17)	33.21
61	68	58	PO	f	1.6(9)	20/18 [0.33]	19(15)	10.59
62	202	132	PO	f	2.3(4)	47/34 [0.07]	27(13)	34.28
63	93	140	PO	4(3)	1.6(9)	15/23 [0.89]	92(46)	14.39
64	10537	10390	2C	0.20(2)	0.73(5) 2.14(4)	347/323 [0.17]	2911(119)	1625.16
65	577	469	PO	0.05(4)	1.78(14)	33/43 [0.87]	138(23)	89.55
66	0	0	X					0
67	1390	1670	2C	0.11(3)	0.78(13) 2.1(2)	68/57 [0.14]	490(54)	262.39
68	112	95	PO	0.05(5)	2.0(5)	22/23 [0.54]	19(8)	17.19
69	257	87	PO	0.14(11)	2.0(4)	31/29 [0.35]	56(13)	39.5
70	658	439	BB	0.17(13)	0.15(5)	38/26 [0.27]	50(38)	100.96
71	441	781	2C	0.2(2)	1.3(3) 3.3(1.5)	63/46 [0.05]	290(69)	97.51
72	218	245	PO	0.04(4)	1.7(3)	39/29 [0.10]	48(12)	34.28
73	213	227	PO	0.48(17)	2.0(3)	39/38 [0.44]	83(19)	32.65
74	147	69	PO	f	1.6(4)	24/22 [0.36]	73(27)	24.39
75	69	42	PO	0.2(2)	2.8(19)	5/4 [0.32]	31(15)	10.9
76	83	109	BB	0.14(14)	0.11(5)	19/30 [0.94]	27(6)	13.07
77	112	99	PO	f	2.1(4)	48/35 [0.07]	21(12)	17.83
78	0	0	X					0
79	228	90	BB	0.6(3)	0.10(3)	45/35 [0.12]	159(127)	34.95
80	228	90	BB	0.5(3)	0.09(3)	45/35 [0.12]	346(309)	38.6
81	94	76	BR	0.14(14)	0.45(25)	18/20 [0.57]	29(21)	14.93
82	0	0	X					0
83	106	68	PO	f	1.2(4)	25/20 [0.21]	33(17)	16.36
84	73	76	PO	f	2.0(4)	23/18 [0.19]	13(10)	11.79
85	528	878	PO	0.05(5)	1.56(17)	41/36 [0.28]	179(38)	96.82
86	76	40	BB	0.2(2)	0.08(8)	7/7 [0.43]	15(13)	11.76
87	65	7	BB	f	0.15(5)	6/7 [0.52]	6.7(5)	10.12
88	70	54	PO	f	2.0(8)	17/13 [0.22]	23(13)	10.95
89	350	399	PO	0.9(4)	1.7(3)	67/51 [0.07]	140(29)	59.22
90	305	282	PO	0.37(16)	1.6(3)	40/55 [0.93]	108(25)	51.52
91	106	75	PO	0.07(7)	3.0(12)	17/22 [0.76]	29(10)	16.69
92	98	73	PO	f	2.0(7)	17/17 [0.43]	13(10)	15.09
93	753	695	2C	0.5(2)	0.13(2) 2.1(4)	44/32 [0.07]	395(124)	127.12
94	46	7	OS				10.5(11)	7.31
95	18	58	PO	f	0.6(7)	5/7 [0.67]	36(27)	3.84
96	369	356	PO	0.10(5)	3.6(6)	61/56 [0.32]	77(15)	63.84
97	247	284	PO	0.4(4)	1.5(6)	21/19 [0.34]	434(257)	41.71
98	409	453	PO	0.41(13)	1.6(2)	75/63 [0.14]	142(27)	62.62
99	188	192	PO	0.04(4)	1.9(3)	51/54 [0.58]	42(12)	29.56
100	250	204	BB	1.3(3)	0.058(9)	28/23 [0.20]	1.4(14) E+5	33.65
101	0	0	X					0
102	11614	12014	2C	0.29(2)	0.98(6) 1.94(5)	374/374 [0.49]	4064(193)	2173.73
103	343	292	BB	0.11(8)	0.11(2)	56/54 [0.39]	50(10)	57.91
104	0	0	X					0
105	18597	18808	can't fit				8227(785)	3480.01
106	40	2	OS				9.0(10)	6.23
107	1476	1232	PO(20)	0.07(4)	2.00(15)	131/118 [0.20]	193(44)	225.17
108	439	504	PO	f	1.97(15)	50/57 [0.72]	73(19)	71.05
109	4281	4795	2C	0.66(9)	0.77(4) 3.1(2)	157/165 [0.65]	2357(293)	654.38
110	31	14	OS				6.9(8)	4.82
111	1950	1775	PO	0.093(10)	1.81(8)	108/85	359(31)	297.15
112	24	6	OS				5.4(6)	3.72
113	13	0	OS				2.9(3)	2.02
114	22	28	IS				9.3(19)	3.37
115	762	568	PO	0.32(13)	0.15(2)	30/20 [0.06]	205(38)	116.25
116	130	212	PO	0.5(2)	3.0(5)	36/41 [0.67]	69(35)	19.87
117	1029	729	BB	0.25(10)	0.132(15)	44/31 [0.06]	500(135)	156.61
118	0	0	X					0
119	383	247	BB	0.12(10)	0.15(3)	46/34 [0.08]	40(10)	58.33
120	275	570	PO	0.24(4)	1.79(19)	19/28 [0.90]	146(31)	49.37

**Table A2.** continued

S	pn source counts	MOS source counts	Mod	$n_{\text{H}}^{22}$	Par	$\chi^2/\text{dof}$ [gf]	$L_{36}^{\text{BF}}$	$L_{36}^{\text{SM}}$
121	943	634	BB (20)	0.35(11)	0.12(2)	83/69	434(71)	143.74
122	282	137	BB	f	0.16(2)	43/45 [0.57]	15(4)	42.91
123	773	4156	2C	0.60(11)	0.94(8) 3.4(5)	84/76 [0.24]	2376(389)	249.8
124	135	100	PO	0.08(8)	1.6(6)	32/37 [0.68]	36(12)	20.95
125	314	371	PO	0.24(8)	1.60(17)	49/42	123(23)	51.03
126	173	662	PO	0.25(8)	2.1(2)	53/42 [0.12]	276(86)	71.72
127	49	76	PO	0.2(2)	3.3(1.9)	7/4 [0.16]	25(13)	7.69
128	420	313	PO	f	1.82(12)	31/40 [0.85]	106(21)	65.76
129	104	98	PO	0.3(2)	3.1(11)	33/24 [0.10]	33(13)	15.97
130	415	332	PO	0.15(5)	1.95(16)	38/39 [0.51]	100(15)	70.12
131	337	219	BB	0.4(3)	0.08(2)	57/47 [0.16]	614(403)	51.61
132	80	48	PO (30)	f	1.7(7)	10/7 [0.22]	19(13)	12.33
133	72	27	PO	f	1.9(9)	7/7 [0.39]	12(10)	11.11
134	0	43	OS				11.3(7)	8.31
135	38	62	PO	0.2(2)	2.5(15)	3/3 [0/40]	19(12)	5.95
136	0	127	PO	0.02(2)	3.1(14)	16/19 [0.62]	36(17)	21.26
137	65	76	PO	0.07(7)	2.0(9)	12/11 [0.35]	17(10)	10.15
138	122	155	PO	0.07(7)	1.5(4)	35/41 [0.71]	56(19)	19.17
139	384	362	PO	f	1.1(2)	39/40 [0.52]	84(29)	60.61
140	124	132	PO	0.13(11)	1.5(4)	27/37 [0.81]	60(17)	19.45
141	127	179	PO	0.7(3)	1.5(3)	52/40 [0.09]	83(23)	19.56
142	196	158	BB	f	0.17(2)	41/30 [0.08]	13(6)	30.73
143	117	91	PO	0.13(6)	3.2(12)	13/24 [0.96]	19(8)	17.93
144	57	85	PO	0.9(8)	1.2(7)	11/14 [0.73]	44(19)	8.82
145	177	146	BB	0.5(3)	0.10(3)	26/28 [0.57]	274(183)	27.21
146	52	35	PO	f	1.1(9)	7/5 [0.25]	33(25)	8.16
147	490	328	PO	f	2.02(12)	38/43 [0.71]	102(19)	76.46
148	0	72	PO	0.7(7)	2.4(19)	9/6 [0.20]	38(23)	14.1
149	69	83	PO	1.9(16)	3.4(16)	15/12 [0.23]	52(29)	10.72
150	101	58	BB	0.3(3)	0.11(7)	5/6 [0.59]	27(8)	15.47
151	177	67	PO	0.34(10)	2.6(4)	41/46 [0.70]	106(27)	27.89
152	171	166	PO	0.014(14)	1.7(3)	37/39 [0.55]	33(12)	26.41
153	0	0	X					0
154	84	61	BB	f	0.10(2)	17/11 [0.11]	17(10)	15.19
155	295	250	PO	f	1.78(15)	27/35 [0.82]	50(12)	45.39
156	27	21	IS				11(2)	4.15
157	13	28	IS				7.9(15)	2.88
158	32	8	OS				7.3(8)	5.08
159	88	94	PO	f	2.1(4)	15/14 [0.39]	21(13)	13.78
160	109	141	PO	0.16(14)	1.9(5)	33/31 [0.37]	35(12)	17.48
161	107	59	PO	0.03(3)	2.2(7)	19/21 [0.60]	25(10)	16.88
162	11	1	OS				2.5(3)	1.76
163	1887	1722	PO	0.03(2)	1.75(8)	60/65 [0.66]	516(38)	294.7
164	512	428	PO	f	1.97(12)	31/31 [0.47]	111(21)	79.72
165	103	103	PO	f	1.9(4)	34/24 [0.09]	25(13)	17.1
166	79	59	PO	0.05(5)	3.0(13)	17/12 [0.14]	23(10)	12.46
167	15	0	IS				6.7(13)	2.46
168	87	99	PO	f	1.9(4)	13/15 [0.57]	17(10)	13.52
169	80	50	PO	f	3.2(8)	8/12 [0.78]	10(6)	12.42
170	35	41	OS				4(3)	6.02
171	118	61	BB	f	0.16(2)	3/14 [0.99]	12(5)	18.33
172	171	137	PO	f	2.1(3)	43/47 [0.62]	40(13)	26.82
173	0	22	IS				10.6(3)	3.88
174	72	43	PO	0.04(4)	1.8(9)	1.2/3 [0.75]	35(17)	11.91
175	15	0	OS				3.7(4)	2.62
176	9	39	OS				2.2(3)	1.55
177	60	76	PO	f	1.5(4)	8/12 [0.79]	21(13)	9.34
178	0	3	IS				1.4(3)	0.59
179	161	96	PO	0.05(5)	1.8(3)	16/30 [0.98]	46(13)	25.19
180	84	82	PO	0.9(8)	1.1(8)	8/12 [0.77]	81(31)	13.12



Table A2. continued

S	pn source counts	MOS source counts	Mod	$n_{\text{H}}^{22}$	Par	$\chi^2/\text{dof}$ [gf]	$L_{36}^{\text{BF}}$	$L_{36}^{SM}$
181	23	28	OS				5.2(6)	3.6
182	126	89	PO	0.03(3)	3.2(9)	16/24 [0.87]	25(8)	19.76
183	45	41	OS				10.2(12)	7.08
184	132	38	PO	0.02(2)	2.0(6)	18/21 [0.67]	60(19)	21
185	0	40	OS				9.6(9)	6.71